Eur. Phys. J. A **1**, 143–149 (1998)

THE EUROPEAN PHYSICAL JOURNAL A

Elastic, inelastic scattering and fusion of the ^{14}N + ^{59}Co system at energies close to the coulomb barrier

C. Muri[1,a], R.M. Anjos[1,a], R. Cabezas[1,a,b], P.R.S. Gomes[1,a], S.B. Moraes[1,a], A.M.M. Maciel[1,a], G.M. Santos[1,a], J. Lubian[1,a,b], M.M. Sant'Anna[1,a], C. Tenreiro[2,c], R. Liguori Neto[2,a], J.C. Acquadro[2], P.A.B. Freitas[2]

[1] Instituto de Física, Universidade Federal Fluminense, Gragoatá, Niterói, R.J., 24210-340, Brazil. fax: +55-21-6204553
[2] Instituto de Física, Universidade de São Paulo, C.P. 20516, S. Paulo, 01498-970, Brazil

Received: 6 February 1997 / Revised version: 1 August 1997
Communicated by C. Signorini

Abstract. Elastic and inelastic scattering differential cross sections were measured in the energy range 30 MeV $\leq$ E$_{lab}$ $\leq$ 55 MeV, for the ^{14}N + ^{59}Co system. Ambiguities of the optical potential derived from the analysis of the elastic scattering data were removed by performing calculations at the radius of sensitivity and by comparison with the available fusion cross section data. A simultaneous analysis of the three mechanisms was performed by coupled channel calculations, and a unique energy independent nuclear potential was found to be able to fit the data. Discussions and comparisons concerning the optical model, the threshold anomaly, full and approximated coupled channel calculations are presented.

PACS. 24.10.Eq Coupled-channel and distorted-wave models – 24.10.Ht Optical and diffraction models – 25.45.De Elastic and inelastic scattering – 25.70.Jj Fusion and fusion-fission reactions

1 Introduction

The development of the study of heavy ion collision mechanisms at near barrier energies, in recent years, is mainly concerned with the rich interplay between different reaction processes and how they influence one another. A theoretical challenge is to describe simultaneously the fusion, quasi-elastic reactions, elastic and inelastic scattering. The search of a unique nuclear potential that describes simultaneously different reaction mechanisms is, therefore, important for the understanding of the complexity of the collision process at low energies.

For the study of the elastic scattering it is usual the use of the optical model. This procedure, however, leads to strong ambiguities. When inelastic scattering data are also available, the simultaneous fit of both mechanisms helps to minimize these ambiguities. Concerning the study of the fusion process, a suitable approach is to consider the coupling of low lying excited states of the colliding nuclei. The introduction of channel eigenstate dependent barriers have the net effect of splitting and lowering the effective Coulomb barrier. The complexity of the full coupled channel calculations has made widespread the use of approximations, as the ones used in the CCFUS code [1].

Another approach to the study of reaction and scattering processes is to replace the many channels theory by a one dimensional barrier penetration model with an energy dependent optical potential [2,3]. The real and imaginary parts of the optical potential are related by a dispersion relation [4]. When the bombarding energy decreases towards the Coulomb barrier, superficial reaction channels are closed and, as consequence, the absorption decreases abruptly. The real potential increases and forms a peak around the top of the barrier. This behavior is called threshold anomaly [2,3]. The coupling of channels and the threshold anomaly are, therefore, different treatments of the same physical problem.

In this paper we present original data for the elastic scattering differential cross sections of the ^{14}N + ^{59}Co system, in the laboratory energy range from 30 MeV to 55 MeV, and for the inelastic scattering to the first excited state of the ^{59}Co, from 30 MeV to 34 MeV. Our group had previously measured [5,6] the fusion excitation function for this system, at bombarding energies from 32 to 56 MeV. Simultaneous fits of the fusion, elastic and inelastic scattering data for the ^{14}N + ^{59}Co system were performed by different methods.

Section 2 describes the experimental set-up used in the elastic and inelastic scattering experiments. In Sect. 3 the analysis of the elastic scattering by the optical model is presented. In Sect. 4, the inelastic scattering is studied by coupled channel calculations. Section 5 is concerned with the fusion excitation function and the differences in its interpretation, when compared with the analysis performed

[a] Fellow of the Conselho Nacional de Desenvolvimento Científico e Tecnlógico - CNPq
[b] Fellow of the Centro Latinoamericano de Fisica - CLAF
[c] *Present address:* Departmento de Fisica, Facultad de Ciencias, Universidad de Chile, Casilla 653, Santiago, Chile

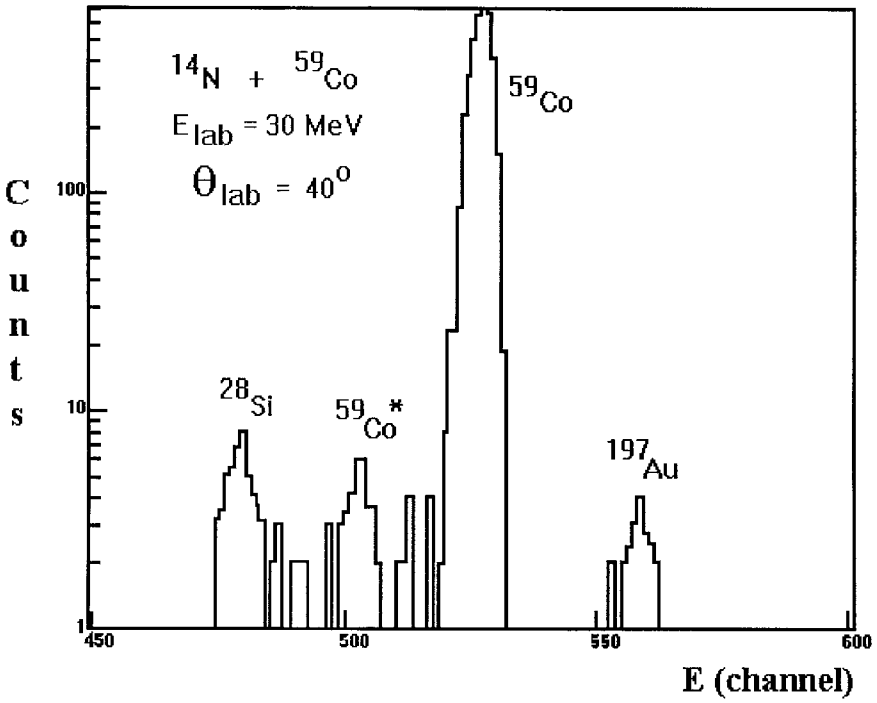

Fig. 1. Typical spectrum for the ^{14}N + ^{59}Co reaction, at E_{Lab} = 30 MeV, θ_{Lab} = 40^0.The expanded region shows the elastic and the first inelastic (1.098 MeV) peaks

with the CCFUS code. In Sect. 6 some conclusions are presented.

2 Experimental details and results

The experiments were performed at the 8UD Pelletron accelerator of the University of Sao Paulo. The ^{14}N beam was extracted from a Duoplasmatron ion source, and its intensity on the target was typically of the order of 50nA. The beam energy range, from 30 MeV to 55 MeV, corresponds to energies near the Coulomb barrier (V_{Blab}= 32.3 MeV [5]). The targets were prepared by evaporation of metallic cobalt, and had thickness of the order of 50 μg/cm^2. They were deposited on 5-10 μg/cm^2 carbon backings. A thin layer of 2 μg/cm^2 of ^{197}Au was also deposited on the target, for calibration and normalization purposes. Some contamination of ^{16}O and ^{28}Si were detected, and were used in the energy calibration of the spectra.

The detection system was an array containing 8 silicon surface barrier detectors with thickness of 100 - 150 mm. Neighbor detectors were separated by 5^0 and the angle determination had a precision of $\pm$ 0.5^0. A monitor was placed at 20 degree with the beam direction. The relative solid angles of the detectors were determined by the Rutherford scattering of ^{14}N on the ^{197}Au target. The energy resolutions of the detectors were of the order of 300 keV(FWHM), good enough to resolve the elastic and first inelastic (1.098 MeV) peaks of the ^{59}Co, as can be seen in Fig. 1.

The differential cross sections for the inelastic scattering ^{59}Co (^{14}N, ^{14}N) ^{59}Co($3/2^-$; 1.098 MeV) were measured for the laboratory energies of 30 MeV, 32 MeV, 33.5 MeV and 34 MeV. For these energies, the angular range was $20^0 \leq \theta \leq 158^0$, and the statistics of each run was determined by the number of counts in the inelastic peak. For higher energies, the angular range was $10^0 \leq \theta \leq 90^0$, and the statistics was determined by the elastic peak. Therefore, only for energies close to the Coulomb barrier, where the coupling of elastic and inelastic channels are expected to be important, there were inelastic scattering data available for the analysis. The uncertainties in the differential cross section data vary from 1% to 10 % for the elastic scattering, and from 10% to 40% for the inelastic scattering.

3 Optical model analysis

For the analysis of the elastic scattering data, the optical model was used by taking the optical potential in the Wood-Saxon form:

$$V_{opt}(r) = -V_0 \frac{1}{1+exp(\frac{r-R_{0V}}{a_V})} - W_0 \frac{1}{1+exp(\frac{r-R_{0W}}{a_W})} \quad (1)$$

where V_0 and W_0 are the real and imaginary depth, and R_{0V}, R_{0W}, a_V and a_W their respective radii and diffusenesses. All the calculations were performed by using the code ECIS [7]. The initial set of optical model parameters (OMP) was taken from the literature [8], obtained for the ^{14}N + ^{56}Fe system, at E_{lab} = 30 MeV. A first series of χ^2 search was performed, when the real and the imaginary strengths V_0 and W_0, and radii R_{0V} and R_{0W} were varied, while the diffusenesses were fixed. Other series of two parameter's fit, V_0 and W_0, were performed, by fixing $R_{0V} = R_{0W}$ as the average value resulting from

Table 1. Examples of Optical Potential Parameters that fit the elastic scattering angular distributions shown in Fig. 2, leading to different reaction cross sections

	V [MeV]	W [MeV]	$R_v = R_w$ [fm]	$a_v = a_w$ [fm]	χ^2 /N	σ_r
			E_{Lab} = 30 MeV			
set 1	393.2	54.86	1.25	0.50	0.45	16.46
set 2	32.8	1.18	1.25	0.70	0.46	8.99
set 3	42.89	0.53	1.25	0.65	0.44	6.41
			E_{Lab} = 32 MeV			
set 1	4.50	2.07	1.45	0.50	0.47	46.82
set 2	2.31	0.35	1.55	0.55	0.50	30.71
set 3	64.73	7.65	1.15	0.65	0.51	37.95
			E_{Lab} = 33.5 MeV			
set 1	41.17	0.62	1.25	0.55	0.67	73.85
set 2	14.6	1.95	1.30	0.65	0.86	88.6
set 3	18.6	3.50	1.25	0.70	0.99	106.3
			E_{Lab} = 34 MeV			
set 1	5.06	2.24	1.45	0.50	0.76	150.2
set 2	95.55	3.59	1.25	0.45	0.82	132.0
set 3	3.57	0.40	1.55	0.50	1.0	101.7

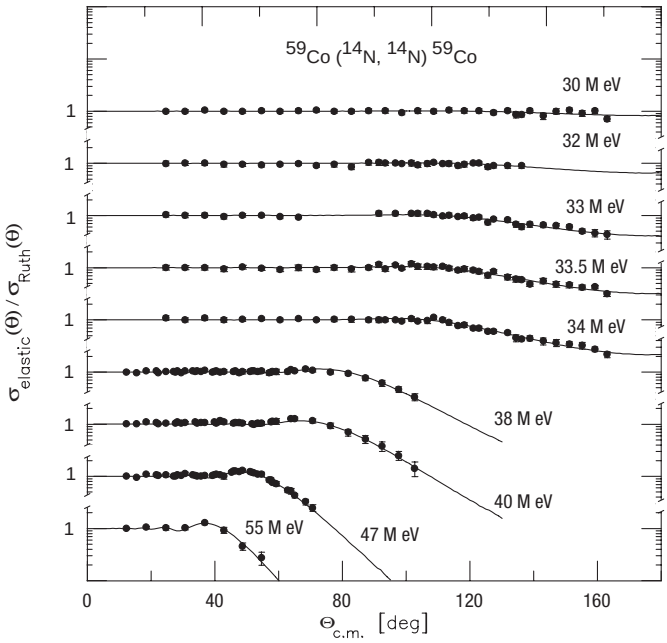

Fig. 2. Elastic scattering angular distributions for the ^{14}N + ^{59}Co reactions. The *lines* show the best fits, within the optical model, using different sets of OMP listed in Table 1

the first fit, and the diffusenesses fixed as different values from $a_V = a_W = 0.40$ fm up to 0.75 in steps of 0.05 fm. With this procedure, for each energy, ambiguous sets of OMP parameters were obtained. Examples of the ambiguities are shown in Table I. The corresponding fits are shown in Fig. 2. It can be seen that the OMP families lead to different reaction cross sections.

Only when the experimental fusion cross sections were used as a strong constraint, some of the ambiguities could be removed. In the fit of the fusion cross section, it was assumed that the absorption into inelastic channels feeds mainly the first excited state and that the other channels are negligible, so it can be assumed that $\sigma_r \approx \sigma_{fusion} + \sigma_{in}$; where σ_r is the reaction cross section, σ_{fusion} is the experimental fusion cross section [5] and σ_{in} is the inelastic cross section of the first excited state, obtained by integrating the experimental differential cross section. When there were no fusion and inelastic cross sections measured at the same energy, an interpolation or extrapolation was made.

Simultaneous fits of the elastic angular distributions and the fusion cross sections were obtained for the sets of OMP shown in Table II. For each of the diffuseness values, one real and one imaginary strength were derived. These OMP families describe equally well the data. For all of them, V_0 gets a maximum at the lowest energies, where one expects to find the threshold anomaly.

In order to reduce these remaining ambiguities, a procedure commonly used [3,9] is the search of the so-called "radius of sensitivity". It corresponds to the radius where potentials, giving comparable fits to the data, have the same value. In Fig. 3, it is shown the radial behavior of the real potential, calculated by taking the optimum V_0 at different diffusenesses from 0.4 to 0.75 fm, for all bombarding energies. The point of intercession of the different potentials corresponds to a well defined radius, R_{SV}, in the region of 10.0 fm. In Fig. 4, it is shown the same as in the Fig. 3, for the imaginary potential. In this case the radius of sensitivity, R_{SW}, is lower than in the case of the real potential. Table III shows the R_{SV} and R_{SW}, at different energies, and their corresponding mean values of 10.01 fm and 7.88 fm. The results for the radii of sensitivity obtained in this system are similar to those already known for ^{27}Al + ^{58}Ni [9], in the sense that R_{SV} and R_{SW} are not necessarily equal to each other.

The points in Fig. 5 are the values of the real and imaginary potentials evaluated at R = 9.45 fm. This value of R was chosen as a compromise, in order to minimize the error bars of both, the real and imaginary potentials. The

Table 2. Sets of optical potential parameters for $R_v = R_w = 1.25$ fm obtained by fitting simultaneously the elastic angular distribution and the fusion cross section data. It was considered that $\sigma_r \approx \sigma_{fusion} + \sigma_{in}$; where σ_r is the reaction cross section and σ_{in} is the integrated inelastic cross section of the first excited state

$E_{Lab}[MeV]$	30.0	32.0	33.0	33.5	34.0	38.0	40.0	47.0	55.0
				set 1		$a_v = a_w = 0.5$ fm			
V [MeV]	120.9	79.25	66.49	61.85	60.56	64.17	38.66	56.26	51.52
W [MeV]	1.22	2.45	2.81	3.50	3.59	7.59	8.59	10.59	11.59
χ^2 /N	0.45	0.52	0.90	0.99	0.82	0.45	0.80	1.08	0.31
σ_r - σ_{in} [mb]	7.39	36.11	69.26	92.50	122.1	423.8	528.1	886.2	1156.0
				set 2		$a_v = a_w = 0.55$ fm			
V [MeV]	91.23	54.97	46.82	42.96	42.61	43.06	38.66	35.39	32.69
W [MeV]	1.22	2.45	2.81	3.50	3.59	7.59	8.59	10.59	11.59
χ^2 /N	0.47	0.54	1.07	1.06	0.90	0.45	0.84	0.97	0.30
σ_r - σ_{in} [mb]	7.44	36.3	69.73	92.0	123.0	425.1	537.0	882.4	1156.8
				set 3		$a_v = a_w = 0.60$ fm			
V [MeV]	65.06	40.37	34.87	31.53	30.89	30.05	24.7	23.35	19.89
W [MeV]	1.22	2.45	2.81	3.50	3.59	7.59	8.59	10.59	11.59
χ^2 /N	0.47	0.54	1.20	1.07	0.76	0.41	0.75	0.98	0.51
σ_r - σ_{in} [mb]	7.11	36.64	70.75	92.81	121.5	428.8	531.8	880.8	1162.6
				set 4		$a_v = a_w = 0.65$ fm			
V [MeV]	42.81	30.64	26.70	23.97	23.6	21.03	15.75	12.46	12.6
W [MeV]	1.22	2.45	2.81	3.50	3.59	7.59	8.59	10.59	11.59
χ^2 /N	0.47	0.53	1.14	1.07	0.76	0.37	0.76	1.78	0.87
σ_r - σ_{in} [mb]	6.98	37.24	71.40	95.0	123.0	434.0	533.9	890.3	1191.4

error bars represent the range of deviation of potentials corresponding to distinct sets of parameters with different values of diffusenesses and roughly the same χ^2. It can be clearly observed an anomalous energy dependence of both potentials at the lowest energies, near the energy corresponding to the Coulomb barrier. The imaginary optical potential W decreases sharply at low energies. The curves in Fig. 5 are the results of the calculations using the dispersion relations in its subtracted form [4] and a simple linear model for W rising from zero to W_0 (in ab-

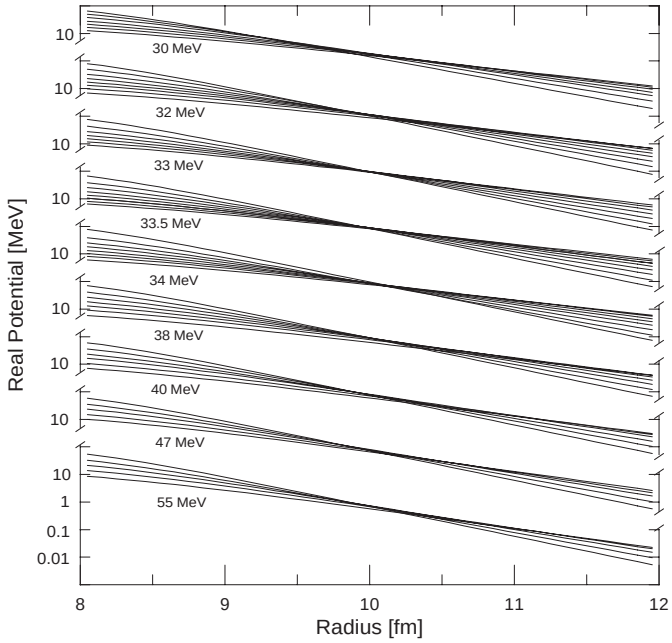

Fig. 3. Radial behavior of the real potential V(r), calculated by taking the set of parameter shown in Table 2 at different diffusenesses. It can be observed a well-defined radius of sensitivity, R_{SV}, in the region of 10.0 fm

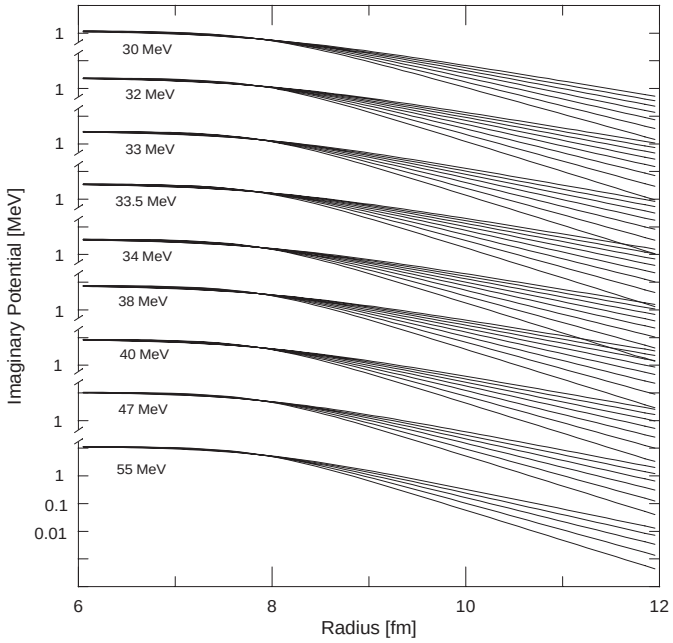

Fig. 4. Radial behavior of the imaginary potential W(r), calculated by taking the set of parameters shown in Table 2 at different diffusenesses. The radius of sensitivity, R_{SW}, is seen to be lower than in the case of the real potential

Table 3. Real and imaginary radii of sensitivity for each energy

ELab [MeV]	R_{SV} [fm]	R_{SW} [fm]
30.0	9.90	7.88
32.0	9.93	7.88
33.0	9.97	7.88
33.5	9.95	7.88
34.0	10.0	7.88
38.0	10.05	7.88
40.0	10.15	7.88
47.0	10.08	7.90
55.0	10.05	7.885
Mean Value	10.01	7.883

solute value) within the interval (E_a, E_b) and a constant value above E_b. The corresponding algebraic expression for the real polarization potential is

$$\Delta V(E) = \frac{W_0}{\pi}(E_a ln|E_a| - E_b ln|E_b|) \quad (2)$$

where

$$E_i = \frac{E - E_i}{E_b - E_a}, i = a.b \quad (3)$$

The adopted values in MeV for W_0, E_a and E_b are 0.2, 24.0 and 34.0. One can see that the derived potentials obey this dispersion relation.

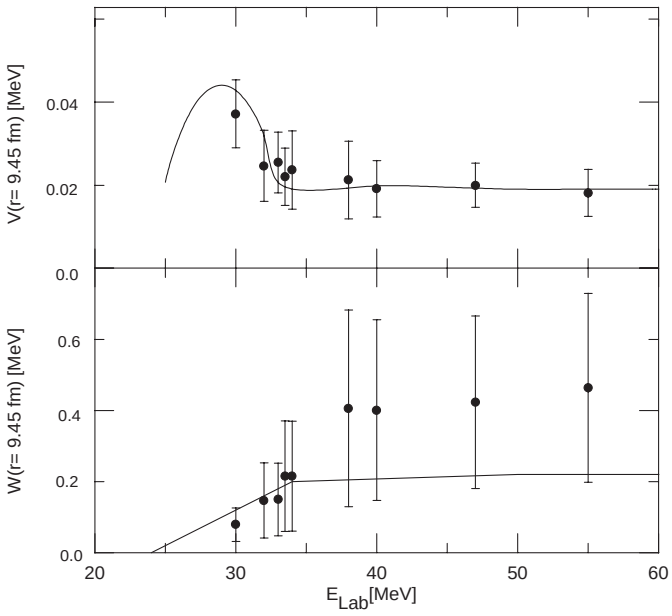

Fig. 5. Values of the real and imaginary parts of the optical potential, at the R = 9.45 fm, an optimum value between the mean real and imaginary radii of sensitivity. The *curves* are the results of the dispersion relation calculations. The threshold anomaly is clearly seen

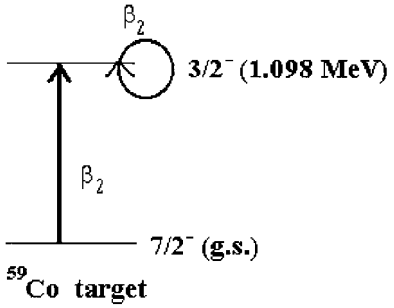

Fig. 6. Coupling scheme used in the full coupled channel calculations

4 Inelastic scattering analysis: coupled-channel calculations

The analyses of the differential cross sections for the inelastic scattering ^{59}Co (^{14}N, ^{14}N) ^{59}Co($3/2^-$; 1.098 MeV) were started by coupled-channel calculations considering a spherical projectile and a deformed target. The coupling scheme considered two states of the target and reorientation effects as shown in Fig. 6.

A quadrupole deformation parameter $\beta_2 = 0.116$ was taken from the literature [10]. The ^{59}Co is a single-hole nucleus in which the unpaired particle is a proton in the $1f_{7/2}$ sub-shell. For the description of its structure, a proton bounded to a deformed axial symmetric core was considered. A description based on the rotational model was employed, using the form factors corresponding to this model. Preliminary calculations have shown that the inclusion, in the coupling scheme, of two or more excited states do not influence significantly the elastic and the inelastic angular distributions of the first excited state. Furthermore, the influence of the reorientation terms was shown to be negligible.

Initially, the real and imaginary nuclear deformation parameters β_{2V} and β_{2W} were taken to be the same and equal to the Coulomb deformation parameter β_{2C}. Optical potentials determined by fitting elastic scattering distributions were used to generate the coupling potentials. In order to obtain acceptable fits, it was necessary to vary the quadrupole deformation parameters to the values of $\beta_{2V} = \beta_{2W} = 0.0718$ and $\beta_{2C} = 0.0724$. During the χ^2 search, the real and the imaginary strength V_0 and W_0 were varied, keeping fixed the geometry ($R_{0V} = R_{0W} =$ 1.25 fm and $a_V = a_W = 0.60$ fm). The results of the fits are shown in the Fig. 7. The full curves represent the fits obtained with the potential parameters listed in Table IV. The corresponding χ^2-values are also shown in this table. One can notice that very good fits were obtained with an energy independent potential. Therefore, the inclusion of the coupling of the first excited state of the ^{59}Co inelastic channel leads to the loss of the anomalous energy dependence of the potential at low energies.

Table 4. Set of OMP obtained by coupled-channel calculations, with $\beta_{2V} = \beta_{2W} = 0.0718$, $\beta_{2C} = 0.0724$, $R_{0V} = R_{0W} = 1.25$ fm and $a_V = a_W = 0.60$ fm

ELAB [MeV]	V_0 [MeV]	W_0 [MeV]	χ^2_{el} /N	χ^2_{inel}/N	σ_{fusion} [mb]
30	28.8	3.59	0.35	0.54	7.69
32	28.8	3.59	0.31	0.14	33.41
33.5	28.8	3.59	0.54	0.32	95.31
34	28.8	3.59	0.43	0.43	127.7

5 Fusion excitation function analysis

Figure 8 shows the fusion excitation function for the ^{14}N + ^{59}Co system. The experimental data were obtained from [5]. The small dashed line is the prediction of the one dimensional barrier penetration model calculated by the FRESCO code [11]. The full line shows the fusion cross sections predicted by the optical model and by the coupled-channel method. The fusion cross section calculations, in both cases, were performed by the FRESCO code. Table IV also shows the calculated fusion cross sections. As the experimental fusion cross sections were also used in the derivation of the potentials based on the fits of the elastic and inelastic angular distributions, a simultaneous fit of the three processes was obtained. The near barrier fusion behavior for this system is, therefore, explained either by the coupling of inelastic channels or by the presence of the threshold anomaly, i.e., they have the same effect on the fusion process.

Simplified coupled channel calculations, with the use of the CCFUS code, were also performed, in order to compare its predictions with the ones obtained with the FRESCO/ECIS codes. The bare potential used in the CCFUS is of the Christensen-Winther type [12]. The first calculation, without any coupling, was done with the parameter ΔV set as 0 MeV, when the depth of the nuclear potential is V_0 = 29.3 MeV. The difuseness parameter used in the CCFUS was 0.63 fm. For these conditions, the predictions for the fusion cross sections were much smaller than the experimental cross sections at high energies. The value of ΔV that fits these data was found to be 30 MeV, with a corresponding nuclear potential strength of V_0 = 59.3 MeV. The results of the calculations are shown in Fig. 8 by the small dashed curve, superposed with those from the uncoupled calculations performed by FRESCO.

The simplified coupled channel calculations were performed by coupling the first three excited states of the ^{59}Co (3/2$^-$, 1.098 MeV, β_2 = 0.116 [10]), (9/2$^-$, 1.90 MeV, β_2 = 0.1054 [13]), (3/2$^-$, 1.460 MeV, β_2 = 0.078 [13]), and the first excited state of the ^{14}N, at 2.31 MeV. The results are shown in Fig. 8 by the large-dashed curve.

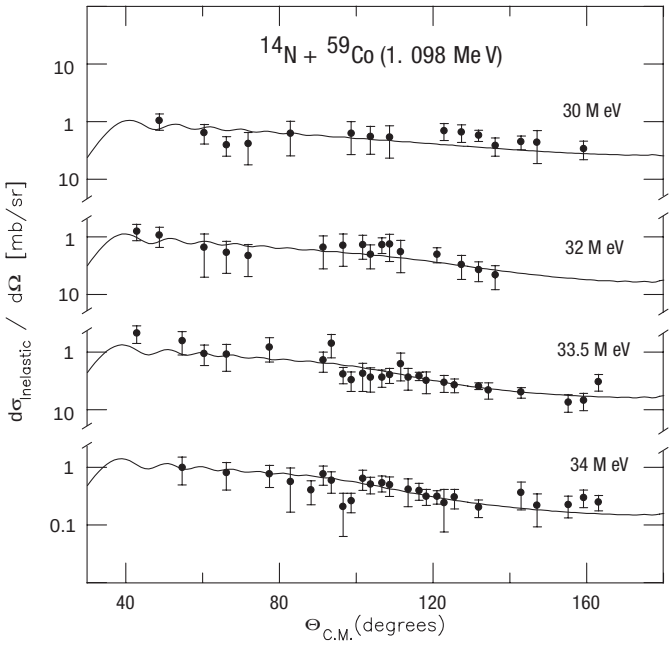

Fig. 7. Inelastic scattering angular distributions for the first excited state in ^{59}Co, at 1.098 MeV. *Solid lines* represent the best fits obtained from the coupled-channel analysis of the data, with the parameters listed in Table 4

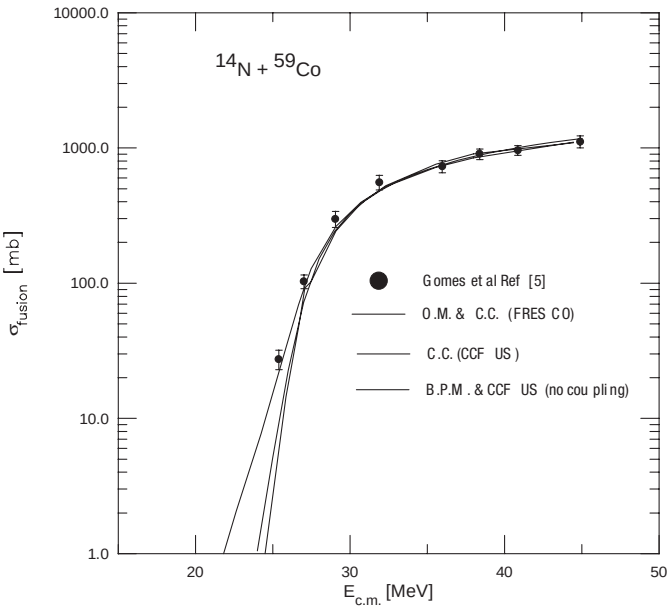

Fig. 8. Fusion cross sections for the ^{14}N + ^{59}Co system. The *points* represent the experimental data [5]. The *full line* represents the predictions using the potentials deduced from the optical model and coupled channel calculation analysis. The *large-dashed line* is the result obtained with the CCFUS code. The *small-dashed line* corresponds to the predictions of one dimensional barrier penetration models by both, the FRESCO and CCFUS codes

One can see that the effect of the coupling of inelastic channels is very small, and it is not able to explain the fusion cross section at the lowest energy. The predictions of the CCFUS are quite different from the FRESCO at sub-barrier energies. If one uses the deformation parameter of the first excited state of the ^{59}Co as $\beta_2 = 0.072$, as it has been derived from the analysis performed by the code ECIS, the fusion enhancement will be even smaller. If one had just the predictions from the CCFUS, one would conclude that transfer channels should also be included in the coupling scheme, in order to be able to fit the fusion excitation function.

This shows that this simplified version of the coupled channel method should be used very carefully because it could lead to wrong conclusions in some cases.

6 Summary and conclusions

Angular distributions of elastic and inelastic scattering were measured for the $^{14}N + ^{59}Co$ system, in the energy range from 30 MeV to 55 MeV. This range corresponds to energies from slightly below the Coulomb barrier to almost twice this value. The first excited state of the target (1.098 MeV) could be well resolved from the elastic peak. At this same energy range, there were available fusion cross sections data, which were used as a constraint to the definition of the optical model parameters that fit the scattering data.

The scattering data were analyzed by two different approaches. The optical model leads to ambiguous energy dependent potentials. The ambiguities were minimized by adjusting the elastic angular distributions and using the experimental fusion and integrated inelastic scattering cross sections. Then, calculations of the real and imaginary potentials, performed at a radius between the mean real and imaginary sensitivity radii show the presence of the threshold anomaly at near barrier energies, satisfying the dispersion relations. In a second approach, the inelastic scattering data was used in coupled channel calculations. From simultaneous fits of the elastic scattering, inelastic scattering and fusion cross sections, an energy independent potential was obtained. As this happens with the coupling of the first inelastic channel of the ^{59}Co, one suggests that this is the only channel that gives a significant contribution to the elastic differential cross section. If the contribution of other channels to the coupling scheme were relevant, the energy dependence of the potential would still remain.

Finally, an important remark must be made, concerning the use of simplified coupled channel calculations for the fusion process, based on codes like the CCFUS, and without any other experimental information apart from the fusion data. It has been argued that this procedure gives good qualitative understanding of the fusion process. However, the present results obtained with the CCFUS code lead to strong different conclusions from the predictions of the ECIS/FRESCO. A clear comparison between these predictions could be done only if the codes used the same kind of potentials. Even so, the present analysis says that, for this system, the simultaneous fit of the three different processes by full coupled channel calculations are achieved without the need of the coupling of transfer channels. Qualitative and quantitative different results were obtained by the CCFUS analysis.

References

1. Dasso, C. H., Landowne, S. and Winther, A.; Nucl. Phys. A**405**, 381 (1983). Dasso, C. H. and Landowne, S.; Phys. Letters B**183**, 141(1987)
2. Nagarajan, M.A., Mahaux,C. and Satchler, G.R.; Phys. Rev. Lett. **54**, 1136 (1985). Nagarajan, M.A., and Satchler, G.R.; Phys.Lett. B **173**, 29 (1986)
3. Satchler, G.R.; Physics Report **199**, 147 (1991)
4. Mahaux, C., Ngo, H. and Satchler, G.R.; Nucl. Phys. A **472**, 591 (1986)
5. Gomes, P.R.S., Penna, T.J.P., Chagas, E.F., Liguori Neto, R., Acquadro, J.C., Pascholati, P.R., Crema, E., Tenreiro, C., Carlin Filho, N. and Coimbra, M.M.; Nucl. Phys. A**534**, 429 (1991)
6. P.R.S. Gomes, T.J.P. Penna, R. Liguori Neto, J.C. Acquadro, C. Tenreiro, P.A.B. Freitas, E. Crema, N. Carlin Filho, M.M. Coimbra; Nucl. Instr. and Meth. in Phys. A**280**, 395 (1989)
7. Raynal, J. ECIS Code, unpublished
8. Williams, M.E., Davis, R.H., Delaune, C.I., Hudson, G.M., Kemper, K.W. and Zeller, A.F.; Phys. Rev. C**11**, 906 (1975)
9. Brandan, M.E., Alfaro, J.R., Menchaca-Rocha, A., Gomez del Campo, J., Satchler, G.R., Stelson, P.H., Kim, H.T. and Shapira, D; Phys. Rev. C**48**, 1147 (1993)
10. Segre, E.; Nuclei and Particles (Benjamin, New York, 1964)
11. Thompson, I.J.; Comp. Phys. Rep. **7**, 167 (1988)
12. Christensen, P.R., Winther, A.; Phys. Lett B**65**, 19 (1976)
13. Peker, L.K.;Nucl. Data Sheets **42**, 457 (1984). Anderson, P., Ekström, L. P., Lyttkens, J., Nucl. Data Sheets **48**, 251 (1986)